Lawrence Berkeley National Laboratory

Title
HEAVY-ION DOSIMETRY

Permalink
https://escholarship.org/uc/item/99d2471t

Author
Schimmerling, W.

Publication Date
1980-03-01

Peer reviewed

Lawrence Berkeley Laboratory

UNIVERSITY OF CALIFORNIA

HEAVY-ION DOSIMETRY

Walter Schimmerling

March 1980

MASTER

Biology &
Medicine
Division

HEAVY-ION DOSIMETRY

Walter Schimmerling,
Division of Biology and Medicine, Lawrence Berkeley
Laboratory, Berkeley, CA 94720

INTRODUCTION

A comprehensive and accurate definition of the physical characteristics of a radiation field is a necessary, but not sufficient, condition for understanding (and predicting) the probability of observing a biological effect. Part of the difficulty of doing this stems from the fact that very often the biological final state accessible to observation is the end result of a long sequence of events following the irradiation, when most of the information has been distributed among many degrees of freedom. Demography is not a very good starting point for the study of photosynthesis, yet that is, in essence, what we are often forced to do.

In some cases, the observed effect only depends on average properties of the radiation field, e.g., the absorbed dose. Thus, for example, we are able to predict that 50 percent of the human population exposed to approximately 500 rads of low LET radiation will die. However, even here there are effects that cannot be attributed to dose, and nobody could say for sure what the LD50 of neon ions for humans might be. It is one of our objectives to ensure that experimental data on this topic never come into existence.

Even within its limitations, the concept of absorbed dose represents significant progress, especially if one takes into account an understanding of the actual averaging procedures used in arriving at it, to which Harald Rossi and his colleagues have contributed so much. The measurement of absorbed dose alone is also sufficiently demanding that an entire subfield has sprung
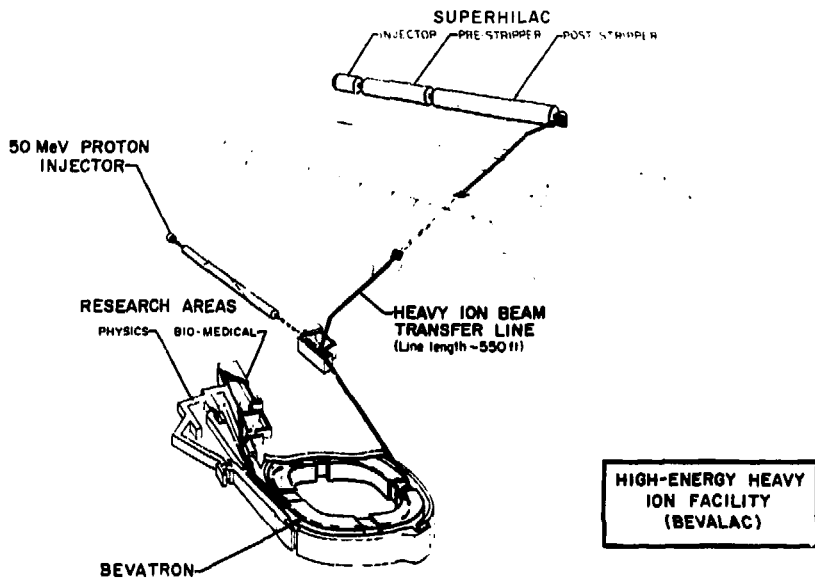
up around it--the science and art of radiation dosimetry. How-
ever, none of us who have an interest in this field are content
with simply measuring one quantity when we know, as stated
above, that a deeper understanding is required.

Accordingly, this lecture will deal with some of the more
important physical characteristics of relativistic heavy ions
and their measurement, with beam delivery and beam monitoring,
and with conventional radiation dosimetry as used in the opera-
tion of the BEVALAC biomedical facility for high energy heavy
ions (Lyman and Howard, 1977; BEVALAC, 1977). Even so, we shall
not be able to discuss many fundamental aspects of the inter-
action of relativistic heavy ions with matter, including
important atomic physics and radiation chemical considerations,
beyond the reminder that such additional understanding is
required before an adequate perspective of the problem can be
attained.

Heavy ion beams were first accelerated to relativistic
energies in the Princeton Particle Accelerator in 1971, follow-
ing suggestions made by Cornelius Tobias thirty year earlier
(Vosburgh, 1973). At present, the only operating facility is
the Berkeley BEVALAC, a schematic diagram of which is shown in
Fig. 1. The SuperHILAC is a heavy ion linear accelerator, which
is operated in a time-shared mode as the injector of the
Bevatron, a weak-focusing synchrotron. The BEVALAC has acceler-
ated beams with masses up to iron. Beams are first accelerated
to 8.5 MeV/nucleon in the SuperHILAC, then bent into an 800-ft
transfer line, where they are transported into the Bevatron for
acceleration up to energies of 2 GeV/nucleon. The beams used
for biomedical research are carbon, neon, and argon, with
energies determined by their desired range in tissue (400 to
500 MeV/nucleon). Dose rates for 20-cm diameter field sizes are
typically between 100 and 300 rad/min, but focused beams can be
obtained with dose rates of the order of 5000 rad/min. The beam
is pulsed, with a frequency dependent on the maximum field
strength required for each beam energy, typically at a rate of
15 pulses per minute. The beam has a microscopic time structure
(that can be smoothed out upon extraction) of typically
40-70 nsec "buckets" every 400-700 nsec.

The BEVALAC Biomedical Facility is an area specially
designated for tumor, tissue, cellular, molecular, neuro-
developmental and space radiobiology, radiography, and radio-
logical physics. The Biomedical Facility has its own control
room, three irradiation caves, and two preparation rooms.
Figure 2 is a floor plan of the facility, showing two of the
irradiation areas. The third irradiation area, known as the
"minibeam" cave (because it is intended for use with narrowly
focused beams), is on top of the shielding where the beam is

SUPERHILAC
INJECTOR PRE-STRIPPER POST STRIPPER

50 MeV PROTON
INJECTOR

RESEARCH AREAS
PHYSICS BIO-MEDICAL

HEAVY ION BEAM
TRANSFER LINE
(Line length ~550 ft)

BEVATRON

HIGH-ENERGY HEAVY
ION FACILITY
(BEVALAC)

3

CBB 729-4520

Fig. 1. Schematic diagram of the BEVALAC high-energy heavy-ion facility.
Reprinted, by permission, from BEVALAC, 1977.
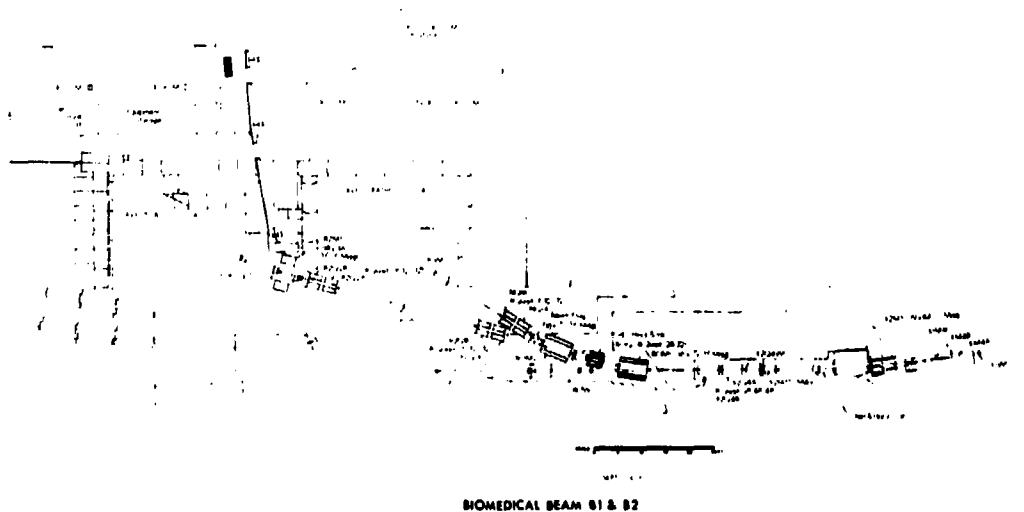
BIOMEDICAL BEAM B1 & B2

XBL 773-7883A

Fig. 2. Floor plan of the BEVALAC Biomedical Facility. Reprinted, by permission, from
BEVALAC, 1977.

incident at an angle of 30⁰ from below. Cave I is intended for therapy and diagnosis, and has a patient positioner and related equipment (Alonso et al., 1979a). Cave II is intended for physical, chemical, and biological research. The minibeam is intended for neurophysiological studies with radiation, and consists of an electrostatically shielded room.


SOME CHARACTERISTICS OF HEAVY ION BEAMS

Physical characteristics of high energy heavy ions that are of interest in their application to biomedical research are summarized in Table 1 (Tobias, 1973). In practice, these properties are influenced by the following factors:

1. The mean free path for nuclear interactions of heavy ions with energies of therapeutic interest is comparable to their range, as shown in Fig. 3. The calculated curves are based on geometrical cross sections and range-energy tables. For the energies of interest here, it may be seen that approximately two-thirds of the incident primary beam will interact with nuclei in the absorbing material to produced secondary fragments. An experimental Bragg peak, illustrating the geometric dose distribution, is shown in Fig. 4, including calculated contributions due to secondary particles (J. Lyman, private communication).

Table 1. Some Important Characteristics of High Energy Heavy Ion Beams

---

1. Stable particles, i.e., intensity, energy, and beam purity are controlled by accelerator.

2. Well-defined range in matter, dependent only on initial energy, i.e., minimal straggling.

3. Reduced multiple scattering which allows the design of sharply defined beams.

4. Well-defined geometrical pattern of energy loss in matter. For monoenergetic beam, leads to increasing dose as a function of depth, up to a peak region located at a depth dependent on the initial energy, with a sharp fall-off at the distal end of the beam.

5. High LET, leading to reduced oxygen enchancement ratio and higher biological effectiveness.
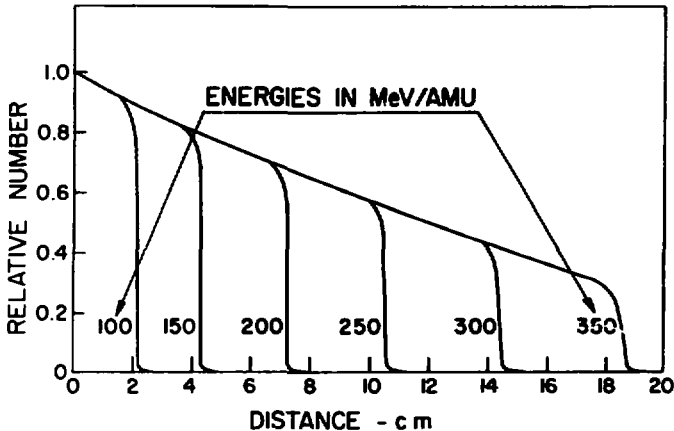
Fig. 3. Mean free path for nuclear interactions of heavy ion with energies of therapeutic interest compared to their range. Reprinted, by permission, from Schimmerling et al., 1973.

2. Multiple scattering. mainly due to many independent small-angle deflections by Coulomb scattering with the nuclei in the medium, results in beam broadening. This can be used to advantage in the beam flattening schemes discussed below, but constrains the design of collimators and air paths in the beam. Secondary fragments, in addition, will contribute a penumbra due to the combination of their own multiple scattering distribution with the angular distribution resulting from nuclear interactions.

3. The beams produced at accelerators are not mono-energetic. When the beam range is controlled by a variable absorber, the initial energy spread is broadened by straggling. The fact that slower particles lose energy at a higher rate results in a slightly asymmetric energy distribution, especially near the Bragg peak, and a broadening of the peak that depends on the amount of absorber interposed.

4. The finite thickness of ionization chambers commonly used to measure Bragg curves results in a measured peak width determined by the average ionization in the chamber.
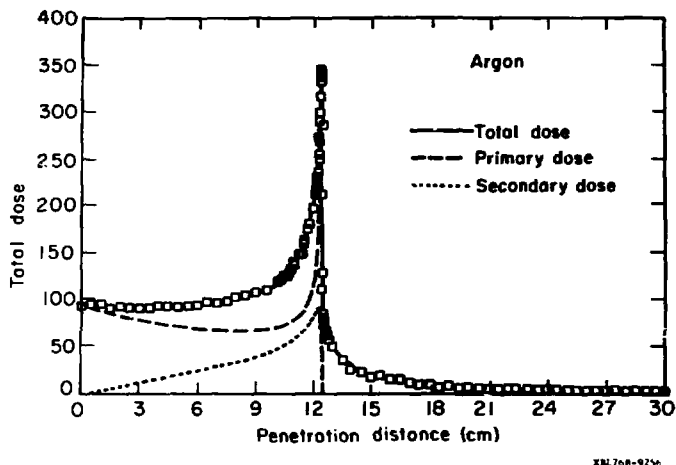
Fig. 4.   Bragg curve for an unmodified argon beam. Reprinted,
by permission, from Lyman and Howard, 1977a.

5. The relative biological effectiveness (RBE) is related to
the LET_∞ as shown in Fig. 5, showing a compilation of results
obtained for cells (E. Blakely, private communication). How-
ever, many sources of variability still exist, and LET by itself
is insufficient to predict biological effects completely.

The inadequacy of LET_∞ as a predictor of biological effect
may be seen more clearly in Fig. 6, showing the inactivation
cross sections for human kidney cells irradiated with carbon,
neon, and argon beams (Blakely et al., 1979). According to model
predictions, the curves should be a fuction of Z^4/β^4, where Z
is the charge of the ion and β its velocity (in units of the
speeds of light, c). In the case of hypoxic cells, the data are,
rather, a function of $Z^4/\beta^{4.6}$, indicating a velocity
dependence of biological effects not described by LET_∞ alone.
Blakely et al. conclude that the description of the biological
effects of heavy ions requires at least three variables, e.g.,
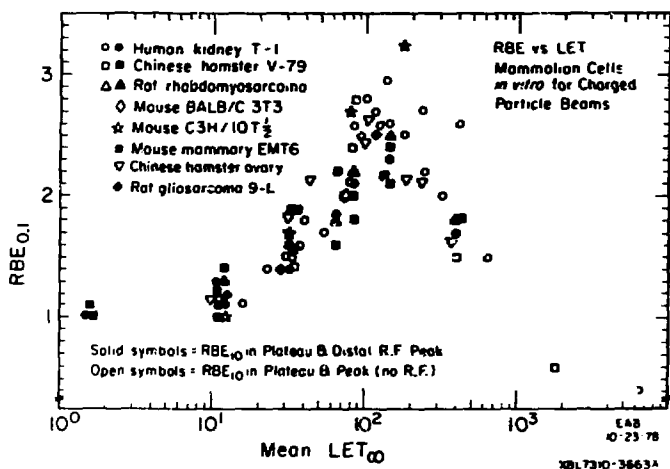fluence, velocity, and charge.

Fig. 5. Relative biological effectiveness as a function of LET
for a variety of mammalian cells. Courtesy of E. A.
Blakely.

The radiation dosimetry of heavy ions thus deals with the
situation depicted schematically in Fig. 7 (with apologies to R.
Magritte): the beam is delivered to a target site, and must be
adequately characterized and monitored in order to provide a
well-defined physical input for biomedical evaluation. The
primary beam, shown coming from the left, interacts with the
components of the beam line used to measure it, and becomes
modified by them. The beam and its reaction products then
interact with the target and its supporting structures, both
directly and indirectly via subsequent scattering.

The incoming beam properties are: the atomic mass, A, and
the charge, Z, of its constituents, the fluence, $\phi_0(x,y)$ in the
plane perpendicular to the beam, the velocity, β (or energy per
nucleon, ϵ), the velocity spread, $\Delta\beta/\beta$ (or energy spread, $\Delta\epsilon/\epsilon$;
sometimes a more useful quantity is the momentum spread, $\Delta p/p$),
the spatial location of the beam, and the angle the beam makes
with the propagation axis, z ($x' = dx/dz$, $y' = dy/dz$).

The material in the beam will consist of beam transport
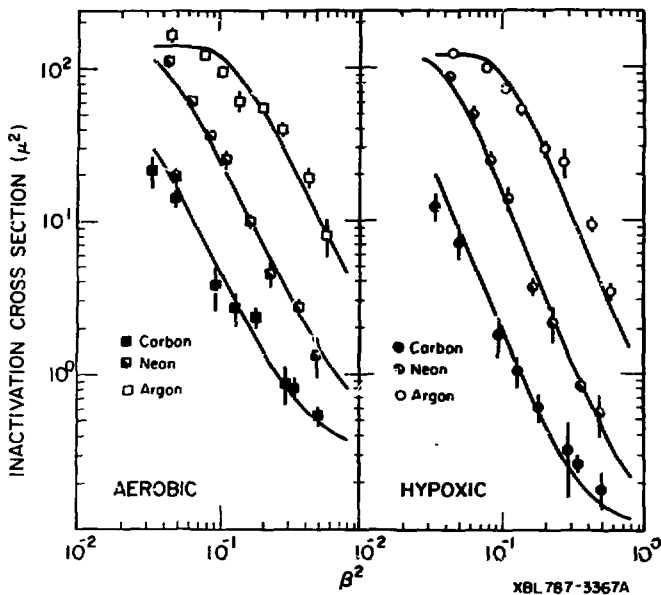elements (magnets), vacuum windows and air gaps, beam delivery

Fig. 6. Inactivation cross sections for human kidney cells
irradiated with carbon, neon, or argon beams.
Reprinted, by permission, from Blakely et al., 1979.

devices (collimators, beam flatteners, ridge filters, variable
thickness absorbers), and beam monitoring and measurement devices
(ionization chambers, wire chambers, scintillation counters).
These materials are characterized, in turn, by their density, ρ,
their total cross section for nuclear interaction, σ_T (or
attenuation length $\lambda = 1/n\sigma_T$, where n is the number of
nuclei/cm^3), various differential cross sections describing the
angular and energy distributions of nuclear interaction
secondaries, denoted by $d^2\sigma/d\epsilon dE$, their radiation length L_{rad}
(a thickness of material relating to multiple scattering), the
average ionization potential, I_{ave}, that enters into the
stopping power, and their own atomic mass, A_T, and number, Z_T.

Quantities that relate to the interaction of the beam with
the material in the beam line are the range, R, which can be
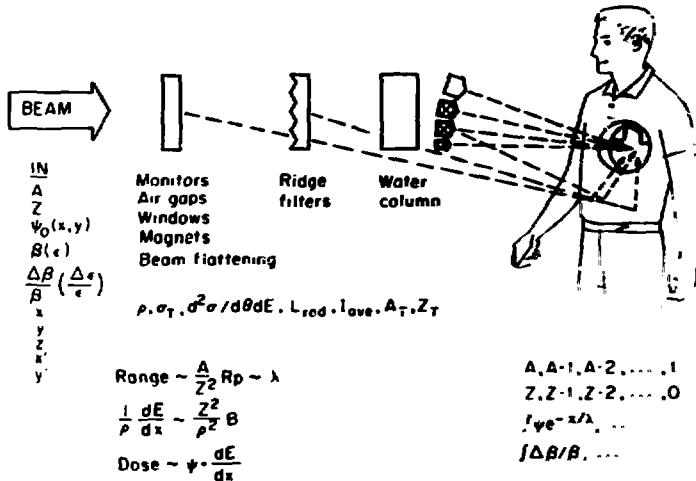scaled to a good approximation as $(AZ^2)R_p$ (R_p = range of a

Fig. 7. Schematic of heavy-ion irradiation arrangement showing the beam and material properties relevant for radiation dosimetry. The integral signs are only used as a mnemonic to denote the thick target attenuation and velocity degradation.

proton with the same velocity) (Schimmerling et al., 1973), and is, as noted, generally also of the order of magnitude of the attenuation length for the energies considered here, the mass stopping power (since thicknesses are more conveniently measured in g/cm^2), $(1/\rho)(dE/dx)$, which also can be scaled to a good approximation as (Z^2/β^2) with respect to the stopping power of heavy ions with different charge (the logarithmic term in the stopping power formula varies slowly), and the "dose," $D = \rho \cdot dE/dx$. The latter is an approximation to the absorbed dose, since $dE/dx \equiv LET_\infty$, and the existence of charged particle equilibrium cannot always be established.

Finally, the actual beam incident on the target may consist of varying contributions of secondaries, with atomic number Z, $Z-1$, $Z-2$, etc., (experimentally, pickup reactions leading to fragments with $Z+1$, or $A+1$, etc., are not observed, and are not favored kinematically). For each of these species, isotopes with mass A, $A-1$, $A-2$, etc., may also be assumed to exist, and the observed flux and velocity distributions will be the integrated

result of all the interactions. In practice, these contribute a small, but not negligible, amount of the actual delivered dose.

BEAM DELIVERY AND SPATIAL DISTRIBUTION

Beam energies at the BEVALAC Biomedical Facility are selected by specifying certain fixed maximum ranges adequate for research and clinical work (Lyman and Howard, 1977; Alonso et al., 1979a, 1979b). The values used most often are listed in Table 2 (BEVALAC, 1977). The restriction to a fixed set of energies is of considerable practical importance in order to obtain reproducible beam line tunes easily, limiting the number of necessary ridge filters, and allowing intercomparison of data obtained in standard beam configurations.

Table 2.   Commonly Used Beams at the BEVALAC Biomedical Facility.

Ion	Nominal Energy (MeV/amu)	Rate (particle/pulse; rad/min)	Range to Bragg Peak (cm)
$^{4}_{2}$Helium (Bevatron)	225	3×10^{8} to 1×10^{9} p/pulse 10 to 50 rad/min	30.4
$^{12}_{5}$Carbon (Bevatron)	400	5×10^{7} to 2×10^{8} p/pulse 20 to 80 rad/min	25.9
$^{12}_{6}$Carbon (BEVALAC)	400	5×10^{8} to 2×10^{9} p/pulse 350 to 1500 rad/min	25.9
$^{20}_{10}$Neon (BEVALAC)	400	2×10^{8} to 1×10^{9} p/pulse 250 to 1200 rad/min	14.6
$^{40}_{18}$Argon (BEVALAC)	500	2×10^{7} to 5×10^{7} p/pulse 200 to 500 rad/min	12.3

Circulating beam in the Bevatron is extracted by means of a resonant extraction system, and provides a "spill" length of up to 1500 msec per Bevatron pulse. Shorter spill can be provided without RF structure. The beam size at the object focus F1 is about 3 cm high, and may be reduced by collimation. The energy spread of the extracted beam is approximately 0.3 percent (BEVALAC, 1977).

The residual range of the primary beam energy can be reduced, in order to accommodate the requirements of different irradiations, by inserting an absorber in the beam. A variable absorber is used to meet these varying requirements. Figure 8 shows a schematic diagram of the 15-cm diameter variable water column used at the BEVALAC Biomedical Facility. The maximum depth is 30 cm of water, variable by computer or manual control. The minimum thickness is the 0.6 cm of the lucite windows. The window is moved by a piston driven by a stepping motor, and is read out to 0.1 mm ± 1 digit.

Another possible design, used for the minibeam area (Schimmerling et al., 1977a), is shown in Fig. 9. This design is based on a double wedge, with some advantages due to its simplicity, lower cost, faster response, and easy exchange of
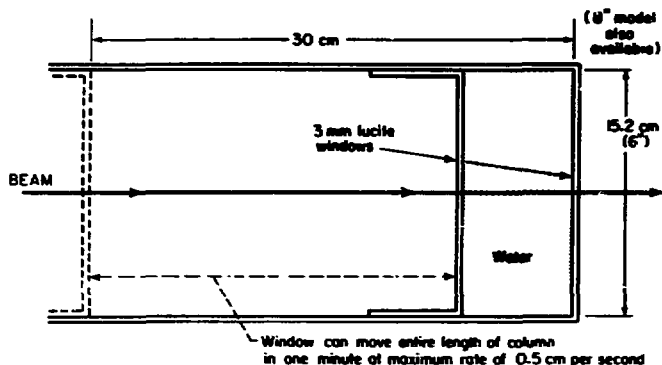
XBL 7610-4131

Fig. 8. Diagram of variable water absorber. Reprinted, by permission, from BEVALAC, 1977.

Fig. 9. A double-wedge variable absorber. Reprinted,
by permission, from Schimmerling et al., 1977a.

absorber material. Its disadvantages are the limited dynamic
range, due to the minimum thickness required in the thinner
wedge, and the maximum practical dimensions of the larger wedge.
A double wedge is, of course, necessary in order to present a
constant thickness surface to the finite beam spot. It is
possible, and often necessary, to obtain a dose distribution in
the target volume (e.g., a tumor region) that differs from that
shown in Fig. 4. Such a distribution may be synthesized by
shifting the range of the particles in a time short compared with
that of the irradiation. The desired dose distribution in the
target volume will then be the time-averaged superposition of
Bragg curves of the type shown in Fig. 4.

There are several means of accomplishing this goal. For example, Tobias (private communication) has suggested the use of a wedge, performing a programmed motion under computer control, to obtain the desired dose distribution curve, since the faster response of this type of variable absorber is required for implementing the concept. At the present time, prescribed dose distributions are achieved with the use of spiral ridge filters, a photograph of which is shown in Fig. 10. These consist of a brass plate with a precisely machined spiral groove. The exact shape and depth of the groove determine the form of the spread Bragg curve.
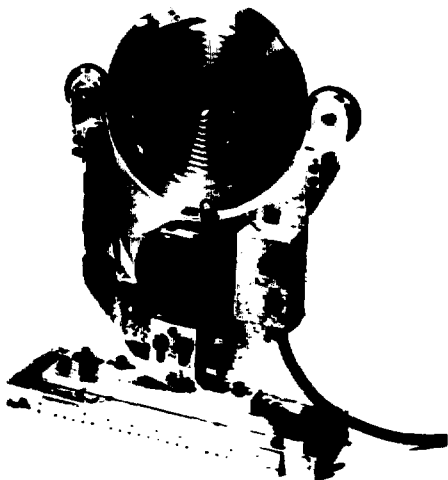
CBB 759-6500

Fig. 10. A spiral ridge filter. Reprinted by permission, from BEVALAC, 1977.

Examples of such spread Bragg curves are shown in Fig. 11 for carbon, neon, and argon beams with "short" (~15 g/cm^2) and "long" (~25 g/cm^2) ranges, and for "narrow" (4 g/cm^2) and "broad" (10 g/cm^2) spreads. The shape of these curves is not flat (isodose), but falls off at the distal end to compensate for the greater RBE, and to yield a constant biological effect (isoeffect criterion). It should be noted that RBE is a function of the biological end point, and therefore the ridge filter will not result in isoeffect curves for different end points (i.e., cell-survival level). As may be evident from Fig. 6, this is true a fortiori for aerated and hypoxic cells--an isoeffect curve for one will not in general be an isoeffect curve for the other.

The spiral ridge has a "dead spot" at the center, where the groove cut ends. For radiobiology experiments, which in general do not require very large beam spots, this problem is circumvented by positioning the filter off-axis from the beam. This is not possible for the large beam spots used in therapy, and the dead region is blocked out by the second scatterer of the beam flattening system described below.

In addition to obtaining a prescribed dose distribution in depth, it is also necessary to define the lateral distribution of the beam. In practice, the simplest way of accomplishing this is by generating a uniform transverse distribution and shaping it to the final contours with collimators. The lateral spreading of the beam into a uniform field is done with the scattering-foil occluding ring system developed at Harvard (Koehler et al., 1977), and at the Berkeley 184-inch Synchrocyclotron (Crowe, 1975). A lead foil, typically 0.6-cm thick, located 10 m upstream of the target volume, scatters the beam into a symmetric Gaussian distribution. A second scatterer, consisting of the ridge filter, an additional 4-mm brass plate, a central brass cylinder, and a concentric brass ring, is positioned approximately 4 m downstream of the first scatterer. The central brass cylinder and the concentric ring block out the central region and an eccentric portion of the Gaussian distribution. The brass plate on the filter acts as a diffuser, filling in the blocked-out regions, so that, after traversing the path to the target, the beam profile is completely flat with an intensity variation of no more than 2 percent over the entire 20-cm diameter field. Approximately 40 percent of the original beam intensity lies within this field, thus providing better beam utilization than would be possible by blowing up the beam size and selecting a uniform central region with collimators. A photograph of the assembled ridge filter with occluding rings is shown in Fig. 12.

Operation of this system requires great alignment accuracy, and several alternatives are under study and development. One
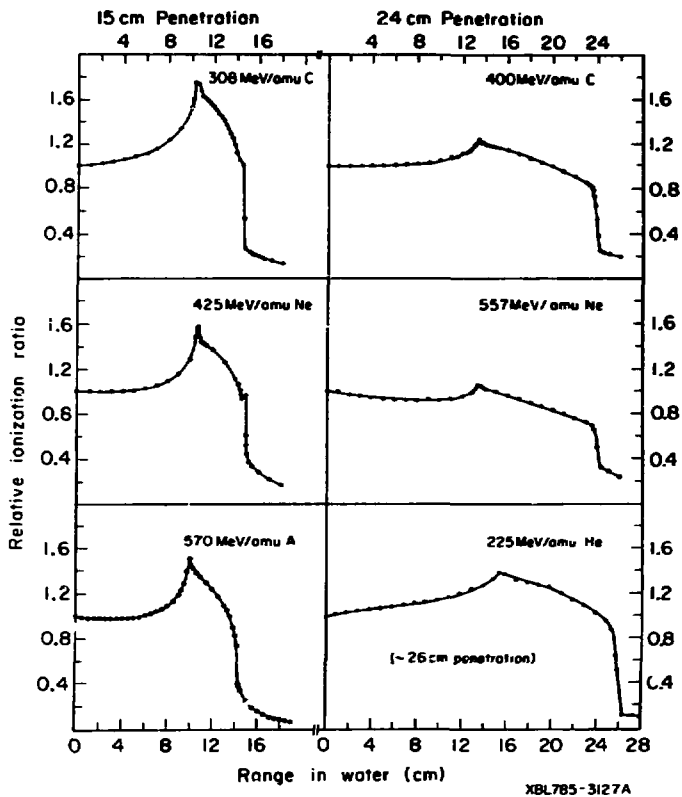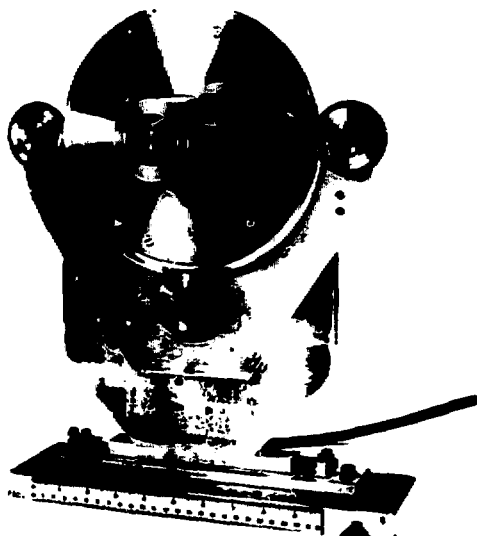
Fig. 11. Bragg curves spread with a ridge filter for different
          incident beam energies and filter range. Reprinted, by
          permission, from, Lyman and Howard, 1977a.

CBB 759-6498

Fig. 12. A spiral ridge filter covered with an
occluding ring. Reprinted, by permis-
sion, from Lyman and Howard, 1977a.

such an alternative is the use of a beam "wobbler," shown
schematically in Fig. 13 (Alonso, private communication). The
device consists of a rotating dipole field, provided by a
stationary sextupole magnet, which sweeps the beam in a circular
pattern to fill in a ring-shaped region, and is turned off to
fill in the central region. Further development will ultimately
lead to a full three-dimensional, computer-controlled scanning
system, receiving its input from treatment-planning and CT
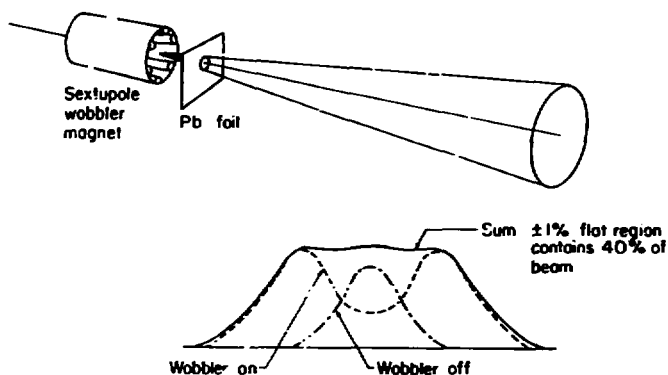
Fig. 13. Beam delivery wobbler system. Courtesy of J. Alonso.

scanning computers. A prototype scanning magnet and power supply have already been constructed. A schematic diagram of the concept is shown in Fig. 14.

Verification of the beam flatness can be accomplished approximately with the concentric-ring ionization chambers described below. For greater accuracy, exposed photographic emulsions and densitometry scans had to be used until recently. This involved six to eight exposures covering a dose range of 1:100, so that a dose vs. film density calibration was obtained simultaneously.

This procedure is time-consuming and cumbersome, and has led to the development of a multiwire, multiplane proportional chamber for reconstruction of beam profiles. The instrument, called MEDUSA (Alonso et al., 1979b), integrates the charge collected from a single beam pulse on capacitors connected to each of the 64 signal wires in each of the 16 planes. The planes are rotated at equal intervals around 180°, perpendicular to the beam. The integrated charge profile from each plane con-- stitutes a projection of the beam intensity (but not of dose!). The beam profile is reconstructed from the 16 different projections, using algorithms developed for CT scanning. Ultimately, reconstruction is expected to take 2 seconds, sufficient to
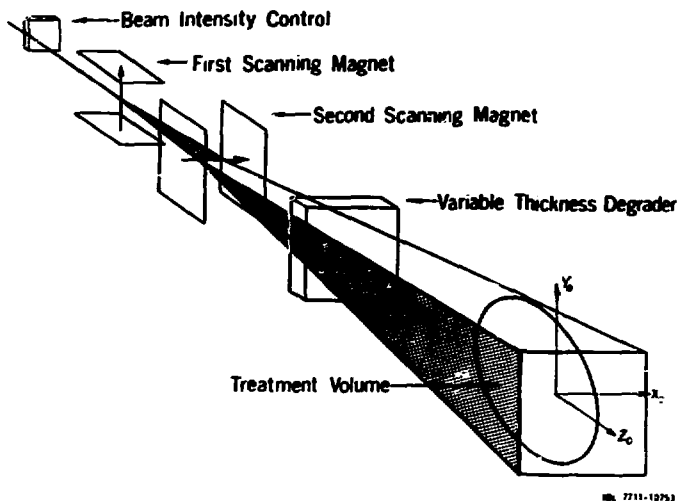
Fig. 14. Schematic depiction of a three-dimensional scanning
method. Reprinted, by permission, from Lawrence
Berkeley Laboratory Report LBL-7230.

enable interactive beam tuning. Accuracy of the device is
expected to be better than 0.5 percent intensity resolution. A
photograph of the assembled chamber is shown in Fig. 15, and a
reconstructed beam profile is shown in Fig. 16. The beam profile
was obtained with a copper bar and lead brick placed in front of
the chamber. The sharpness of the edges is a good indication of
the spatial resolution of the instrument (10 percent to
90 percent in 3 pixels) and its ability to reconstruct asymmetric
patterns.

DOSIMETRY

It must be emphasized that dosimetry serves both a predic-
tive and an archival function. It is as important to know the
physical characteristics of beams that will be delivered as it is
important to know the characteristics of beams that have been
delivered. Most of the methods described in this section are
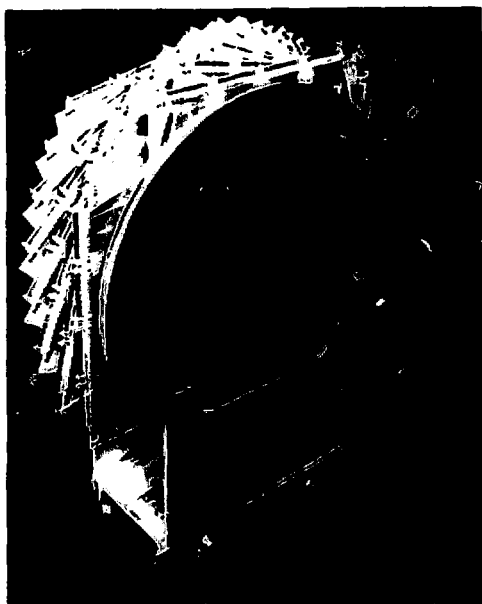
CBB 783-3335

Fig. 15. MEDUSA chamber. Reprinted, by permission,
from Alonso et al., 1977b.

used for beam verification. Instruments used for routine opera-
tion at the BEVALAC presently measure dose intensity distri-
butions. Microdosimetric measurements have been made, and are
described in other lectures of this course. Other studies of
beam quality will be discussed below.

The most useful monitor for the heavy ion beams is a parallel
plate ionization chamber. The basic ionization chamber used in
biomedical dosimetry at the BEVALAC (1977) consists of three
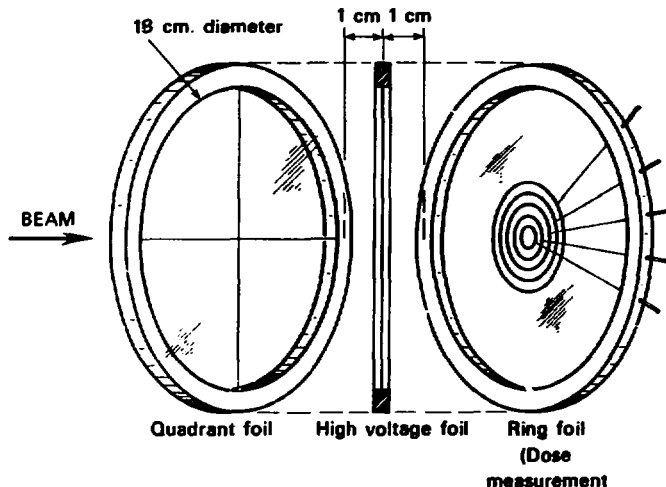foils mounted on insulating frames in a gas-tight aluminum
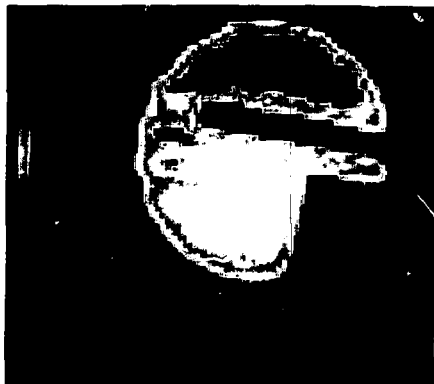
Fig. 16. Reconstruction of a radiation
field obstructed by a rectangular
metallic absorber after smoothing
the raw data. Reprinted, by per-
mission, from Alonso et al., 1977b.

housing, as shown in Fig. 17. The three foils are a quadrant
foil, a high voltage foil, and a concentric, ringed foil. The
foils are constructed of thin plastic membranes and gold plated
on both sides in the appropriate pattern. The charge collected
by the various electrodes is integrated and measured by linear,
seven-decade voltage-to-frequency converters.

The signals from diammetrically opposed quadrants in the
quadrant foil can be added and modulated with a sine-wave
generator. When the resultant signals are applied to the x- and
y-sweeps of an oscilloscope, the resultant Lissajous pattern is a
circle or ellipse with semi-axes or radius proportional to the
beam intensity, centered on a location that can be referred to
the beam position. In this way, a continuous indication of
relative intensity and position is obtained.

18 cm. diameter

1 cm 1 cm

BEAM

Quadrant foil   High voltage foil   Ring foil
                                      (Dose
                                      measurement

XBL 7611 9940

Fig. 17.   Ionization chamber foils. Reprinted, by permission,
            from BEVALAC, 1977.

The ringed foil allows monitoring of the dose as a function
of radial distance from the beam axis (Lyman et al., 1975) as
well as a measurement of total dose (when the beam spot is
smaller than the active area of the chamber). A photograph of
the disassembled chamber is shown in Fig. 18.

Figure 19 shows a scale drawing of the ionization chamber
used in Princeton (Schimmerling et al., 1976). This chamber is
similar in geometry, and does not feature multiple electrodes.
Emphasis in this design was placed on eliminating the use of
adhesives that could contaminate the filling gas with organic
vapors. Also noteworthy in this design are the provisions for
vacuum baking for initial cleanup, and the pierced foils at each
end of the chamber, used for damping microphonic noise, to which
this type of instrument is extremely susceptible.

CBB 752-1328

Fig. 18. Disassembled components of the ioniza-
tion chamber used in the LBL Biomedical
facility (drawn schematically in Fig. 17.
Reprinted, by permission, from BEVALAC,
1977.

The Berkeley chamber is flushed with dry nitrogen gas, while
the Princeton chamber used argon. The choice of filling gas is
determined by the desire to have a well-defined material as well
as by the advisability of using the chambers in the electron
collection mode. The latter, especially, is important in order
to deal with the high ionization of heavy ions, and to collect
the produced charges in a time which is short relative to recom-
bination lifetimes. Nitrogen and argon have low electron
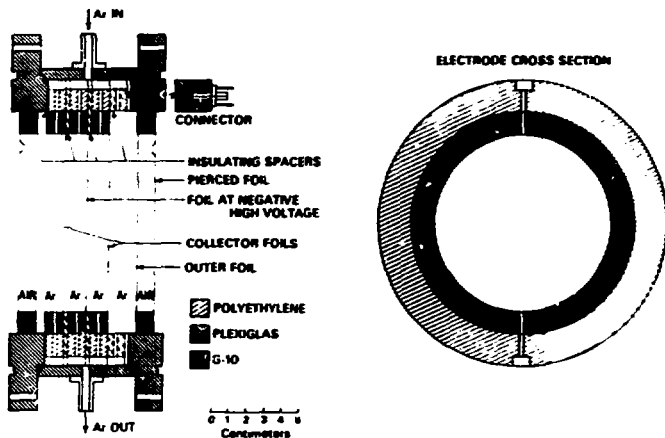
Fig. 19. Scale drawing of the ionization chamber used at
          Princeton. Reprinted, by permission, from
          Schimmerling et al., 1976.

affinities, and are useful for this reason. When ionization
chambers, such as the one shown in Fig. 19, are used in pulse
mode, it is further important to minimize electron collection
times to ensure proper linearity (collection of all the produced
charge) and maximize counting rates. In that case, propane and
methane give the highest electron mobilities and are the filling
gas of choice. Tissue-equivalent gases that have the same
electron density as muscle tissue are also used in order to avoid
errors introduced by the calculation of absorbed dose in tissue
from the measured ionization.

The measured charge, or ionization, in the chamber can be
related to the energy loss in the chamber and, hence, to the
absorbed dose, if the average energy required to produce one ion
pair, W, is known. This quantity is not easily calculated in an
accurate form (Myers, 1968), and has become the object of revived
theoretical and experimental interest (Dennis, 1972; ICRU, 1979)
in the light of its importance for charged particle dosimetry.

The experimental determination of W requires an independent measurement of beam intensity in order to determine the average ionization per incident beam particle. W in argon was determined (Schimmerling et al., 1976) for nitrogen ions of 520 MeV/u by using carbon activation detectors to monitor the beam passing through the ionization chamber, based on the measured $^{12}C(^{14}N,x)^{11}C$ cross section (Skoski et al., 1973). The value of W obtained, 26.2 ± 1.8 eV/i.p., was in good agreement with the value of 26.3 ± 0.1 for alpha particles in argon (Myers, 1968). Stephens et al. (1976) have used thermoluminescent dosimeters to measure the fluence of 250 MeV/A carbon ions, and obtained a value of 36.6 ± 0.7 eV/i.p. for W in the nitrogen gas used at the BEVALAC. Subsequent measurements report values of 35.3 ± 1.5 eV/i.p. for neon at 375 MeV/A and 34.6 ± 1.4 eV/i.p. for 429 MeV/A argon ions in nitrogen (Thomas et al., 1978). The difference between these values is not statistically significant, and the authors of this work conclude that the average value of $W = 35.2 \pm 0.9$ eV/i.p. in nitrogen may be taken as the best value presently available, independently of particle charge or velocity. This is to be compared with the value of $W = 34.9$ eV/i.p. used for routine BEVALAC operations (1977).

All these measurements rely upon a two-step procedure to establish the absolute beam fluence. In a first step, the method is calibrated at low intensities, where the signal-to-noise ratio in ionization chambers operated in the current mode is too small for reliable comparison. In this mode scintillation counters (Schimmerling et al., 1976) or nuclear emulsions (Skoski et al., 1973; Stephens et al., 1976), can be used for absolute counting. The second step, at intensities within the operational range of the ionization chamber, compares the secondary standard (activation foils, thermoluminescent dosimeters, etc) with the ionization current. Figure 20 shows the typical efficiency of thermoluminescent detectors relative to ^{60}Co gamma rays and comparison with some theoretical models (Patrick et al., 1976).

It is possible to circumvent this two-step procedure by using the ionization chamber in a pulse mode (Epstein et al., 1971) and counting beam particles directly. This is done in the fragment dose experiments described below. Preliminary measurements (Schimmerling et al., unpublished results) show agreement between the value obtained for 525 MeV/A argon ions in propane and the value calculated using Bragg's rule, $W = 29.6$ eV/i.p. Similarly, measurements by Goodman and Colvett (1977) have shown that the value of W for argon ions in air and TE gas is not significantly different from that obtained with a ^{137}Cs source. It seems safe to conclude that, except perhaps for a narrow region beyond the Bragg peak where the velocity of the heavy ions becomes comparable with that of orbital electrons, W values of heavy
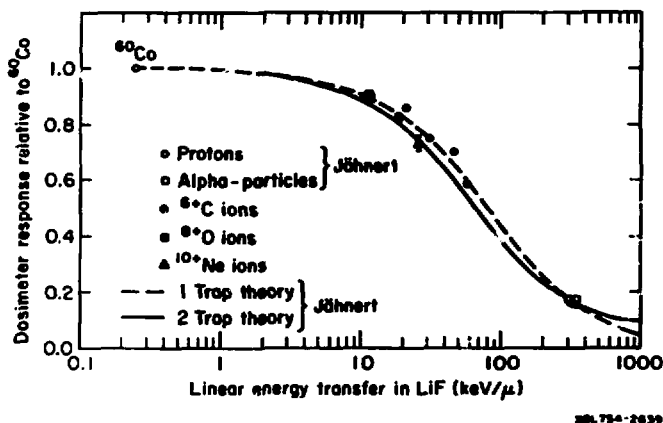
Fig. 20. Efficiency of thermoluminescent detectors relative
to ^{60}Co. Reprinted, by permission, from Lawrence
Berkeley Laboratory Report LBL 6710.

ions differ by less than 5 percent from those of lighter charged
particles.

The accuracy of absolute dosimetry is dependent upon W, a
knowledge of the stopping power, the dimensions of the ioniza-
tion chamber, and the method of charge collection. The accuracy
of W measurements is, as we have seen, not much better than
5 percent. Stopping power cannot be calculated to an accuracy
better than a few percent at the present time, and experimental
measurements are also not more accurate, for the energies and
ions considered here. Improvements in these accuracies would
require quite sophisticated and fastidious experiments. Thus,
the accuracy of absolute physical dose determinations cannot be
assumed to be better than 5 to 10 percent.

Fortunately, evaluations of the merits of radiation therapy
rely on relative observations and reproducibility of dose
measurements can be attained at the few percent level or better,
as evidenced by preliminary results of recent intercomparisons.
These comparisons utilized 1 cm^3 tissue-equivalent ionization
chambers to eliminate sensitivity to field shapes, and referred
the measurements to ^{60}Co doses. This work is being performed

under the auspices of the Charged Particle Dosimetry Group
(CPPDG) of the American Association of Physicists in Medicine.

Figure 21 shows the complete panoply of instrumentation used
for routine high-energy heavy ion dosimetry at the BEVALAC,
mounted on a standard alignment bench. The beam is incident from
the left, and the instruments in the beam path, from left to
right, are: collimator, upstream ionization chamber (for
intensity normalization), scintillators, collimator, spiral ridge
filter, variable water absorber, aperture holder, downstream
ionization chamber, remote control sample translator, EG and G TE
ionization chamber, alignment pointer, cross hairs and x-ray tube

CBB 769-8487

Fig. 21.   The instrumentation used for radiation dosimetry at
           the BEVALAC Biomedical Facility. Shown from left to
           right: brass collimator, upstream ionization chamber,
           collimator, spiral ridge filter, variable thickness
           water absorber, aperture holder, downstream ioniza-
           tion chamber, remote control sample translator,
           EG and G TE Ionization chamber, alignment pointer,
           cross hairs and x-ray tube, and a utility fixture
           with a custom-poured collimator. Reprinted, by
           permission, from BEVALAC, 1977.

also used for alignment, and a utility fixture with a custom-
poured collimator. The alignment bench for the minibeam is shown
in Fig. 22, showing the double wedge, ionization chambers, and a
microscope system to be used for on-line studies of cell
function. The microscope is equipped with remote handling
facilities, as well as a movie camera and a videotape unit for
time-lapse photography. The television monitor in the figure
displays a culture of neuroblastoma cells being used by T.C.H.
Yang of LBL for preliminary studies.

The dose measured by the ionization chamber behind the water
column is related to the absorbed dose in samples behind the
ionization chamber by a displacement correction to account for
the material between the sample and the chamber (measured with

Fig. 22.   Photograph of alignment bench used in BEVALAC mini-
beam.   Shown from left to right are: upstream ioniza-
tion chamber of the type shown in Fig. 19, double
wedge, downstream ionization chamber, beam spot film
holder, and microscope system.   Reprinted, by permis-
sion from Schimmerling et al., 1977a.

the water column) and by the ratio of stopping powers in the material and the chamber gas. This procedure has been validated by Goodman an. Colvett (1977) who concluded that the depth-dose distributions measured for high-energy argon ions in a water phantom and in a tissue equivalent liquid were essentially the same, after taking into account the difference in electron densities between the two liquids, at the 5 percent level. Similarly, the depth-dose distribution measured behind the water absorber was equivalent to that measured inside a water phantom. Finally, the results showed no significant difference between dosimetry in air and in tissue-equivalent gas in the cavity of a tissue-equivalent ionization chamber.

NUCLEAR INTERACTIONS AND BEAM QUALITY

As discussed in the Introduction, the mean free path of the heavy ion beams used for biomedical applications is comparable to their range. Thus, secondary and, possibly, subsequent generations of nuclear interaction products can be expected to make a significant contribution to the dose, especially in the vicinity of the Bragg peak and in the spread depth dose distribution. For the purposes of therapy planning, of course, it must be remembered that nuclear interaction products will constitute 100 percent of the exit dose. In addition, it has been shown that biological effect depends not only on the LET, but possibly on the charge and velocity in different ways. Thus, one approach to characterizing high-energy heavy-ion beams in a manner that would eliminate uncertainties about their physical characteristics from the radiobiological evaluation, is the measurement of velocity and ionization spectra for identified fragments as a function of depth.

Preliminary measurements, using only velocity spectra, showed that the present state of knowledge about fragmentation cross sections and their dependence on the incident particle energy is insufficient to permit accurate predictions (Schimmerling et al., 1977b). Estimated cross sections for fragments produced in the interaction of 251 MeV/u nitrogen ions on carbon, based on the semi-empirical model of Silberberg and Tsao (1973) and calculated as described by Schimmerling et al. (1977b), are shown in Fig. 23. These cross sections are generally in agreement with experimental data at the 20-30 percent level down to energies of 150 MeV/u. Data between 20 MeV/u ard 100 to 200 MeV/u are unavailable at present. Such data are required for every element in tissue, or must be calculated by a scaling procedure. In addition, the angular distributions and energy spectra, as well
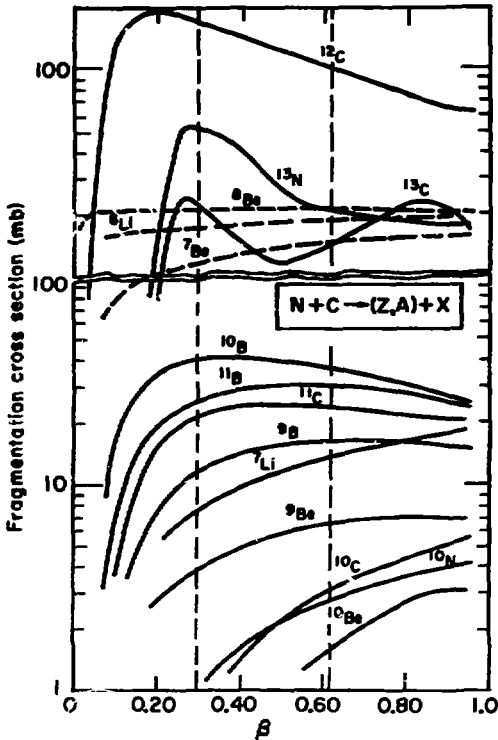
Fig. 23.   Cross sections for producing fragments
           from the interaction of nitrogen ions
           with a carbon target, as a function of
           velocity, estimated from the semi-
           empirical model of Silberberg and Tsao
           (1973). Reprinted, by permission from
           Schimmerling et al., 1977b.

as the multiplicities of light particles (neutrons, protons), must be known for an accurate calculation. Few such data are at present available.

Nuclear physics experiments provide data that are useful for biomedical purposes only after incorporation into cumbersome transport calculations of limited accuracy. Therefore, the approach of obtaining such data directly is currently being pursued at the BEVALAC. Preliminary results (Schimmerling et al., unpublished data), were obtained with the arrangement shown in Fig. 24. R is a variable thickness absorber. The detector consists of a multiwire proportional chamber to measure particle position, a channel plate time-of-flight telescope with a resolution of about 100 picoseconds (Gabor et al., 1975) (corresponding to an energy resolution of about 0.1 percent at low energies), and a pulse ionization chamber for single particle ionization measurements. S_0, S_1, and S_2 are scintillation detectors used to monitor the beam intensity and to impose a range requirement: a signal in all detectors except S_2 indicates that the particle stopped somewhere between S_1 and S_2, and gives a measurement of its range. A photograph of the experimental setup is shown in Fig. 25.
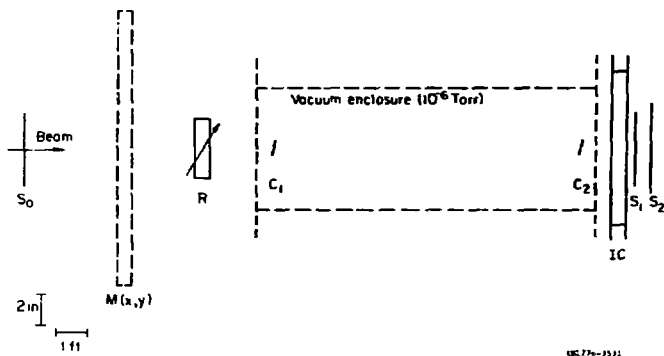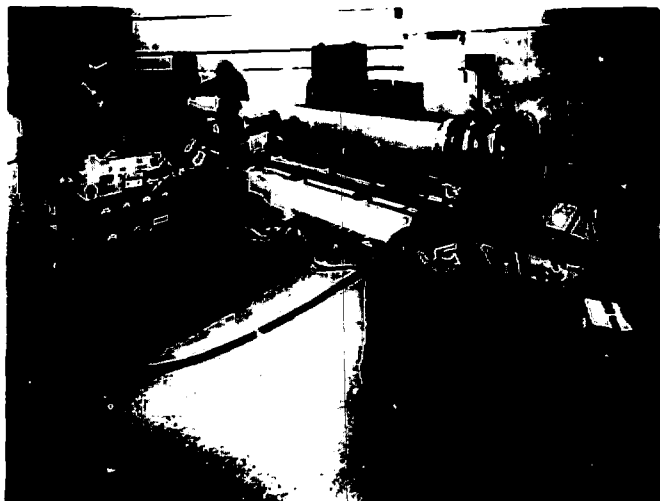

Fig. 24.   Schematic diagram of instrumental arrangement used
for element identification of fragments emerging
from a thick absorber R. S_0, scintillator; $M(x,y)$,
wire chamber; C_1 and C_2 foils of a channel plate
time-of-flight spectrometer; IC, pulse ionization
chamber; S_1 and S_2, range discrimination scintil-
lators.

Fig. 25.   Photograph of experimental arrangement shown in
Fig. 24. The long pipe contains the time-of-
flight spectrometer and is connected to a high-
vacuum pumping system. The beam is incident from
the left.

The purpose of this arrangement was to build an ionization-
sensitive particle identifier with minimum mass, in order to
separate the secondary particles close to the Bragg curve.   The
charge resolution of the ionization chamber is limited by the
statistical distribution of energy losses.   This "Landau tail"
(Rossi, 1952) is, however, limited in a thin ionization chamber
because very energetic electrons (delta rays) can only deposit a
small fraction of their energy in the chamber (Epstein et al.,
1971).   In this sense, the ionization chamber is a "restricted
energy loss detector," and its charge resolution, approximately
7 percent, is much better than would be predicted without this
consideration.   The counting rate of the chamber is limited by
the collection time for the electrons (~3 μsec).   Even though
this is much slower than, e.g., thin plastic scintillators, the
pronounced saturation effects of these place them at a dis-
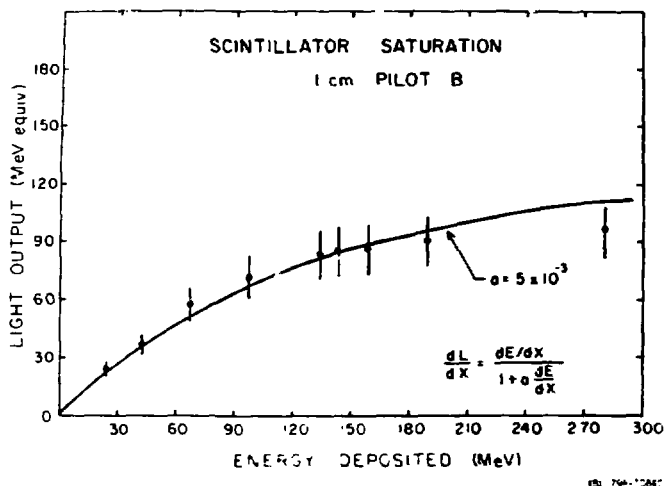advantage with respect to ionization chambers in applications to

Fig. 26. Example of the saturation in scintillator output.
Reprinted, by permission, from Kidd et al., 1979.

heavy-ion dosimetry. Figure 26 shows an example of the satura-
tion in scintillator output (Kidd et al., 1979). In experiments
being set up at this time, a solid-state detector telescope
(Greiner, 1972), with isotopic resolution of the order of
0.2 amu, will be used in conjunction with this apparatus.

A typical time-of-flight spectrum of 525 MeV/A argon beam,
near the end of the argon range, is shown in Fig. 27. Velocity
increases from right to left, with the slowest particles having
the longest flight time (corresponding to the higher channels).
The residual peak of argon can still be seen, as well as the
substantial flux of secondary particles, mixed in the distri-
bution to the left of argon.

Ionization pulse height spectra at a depth of 12.5 g/cm^2 of
Lucite for an incident 525 MeV/A argon beam are shown in
Fig. 28. Cuts on the data were made using the known charge
resolution of the ionization chamber and the calculated
velocity-ionization profile of argon in the detector. The lower
left panel shows the ionization pulse height spectrum without any
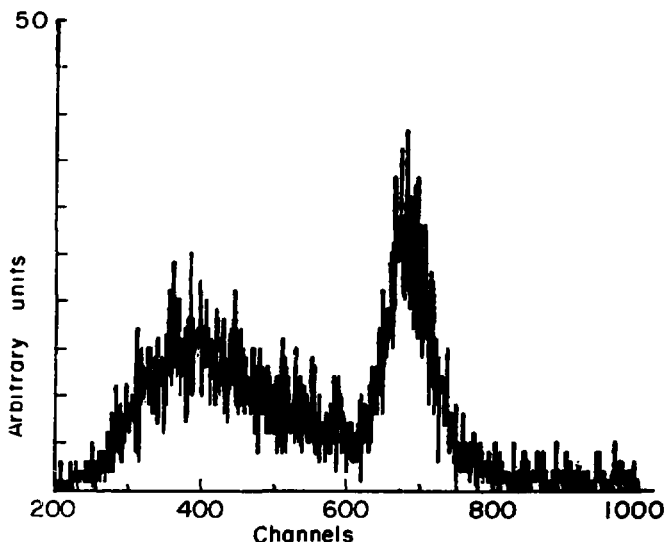
Fig. 27. Time-of-flight spectrum of 525 MeV/nucleon argon
ions after traversing 12.5 g/cm^2 of Lucite. Time
increases from left to right, and velocity corres-
pondingly decreases from left to right.

cuts. The upper right hand panel shows the distribution of all
secondary particles (corresponding to the region left of the
argon peak in Fig. 27). The charge resolution is rather poor,
but some structure seems evident and should be resolved in future
work. Finally, the ionization spectrum for particles identified
as argon is shown in the lower right hand panel of Fig. 28. The
average ionization can be obtained from spectra such as this, and
plotted as a function of absorber thickness to obtain the
separated depth-dose curve for argon shown in Fig. 29.

Near the peak (at 14.6 g/cm^2) in Fig. 29, the data are
adequate to provide a crude estimate of the effect of second-
aries on the dose distribution of argon. Assuming that lower-Z
particles have a mean charge of $Z = 15$, and using the measured
mean velocity, the estimated contribution of lower-Z secondaries
to the dose is 23 percent, at an average LET$_\infty$ of 130 keV/μm. The

XBL 798-10835
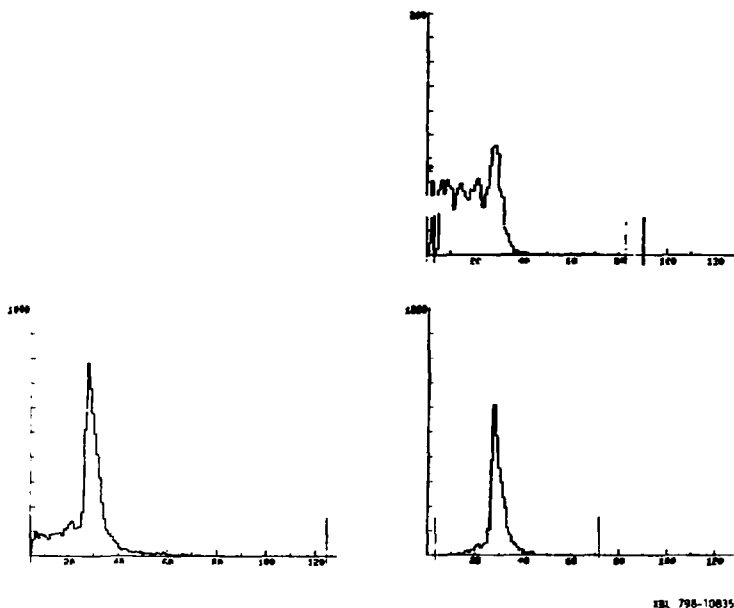
Fig. 28. Ionization pulse height spectra at the exit of 12.5 g/cm^2 of Lucite for a 525 MeV/nucleon incident argon beam.

primary argon is estimated to contribute 39 percent of the dose at this point, at an LET$_\infty$ of 323 keV/μm. Lighter isotopes of argon (e.g., ^{38,39}Ar) and chlorine (e.g., ^{35}Cl) begin to stop in this region, and can be identified with the range requirement. Their contribution to the dose can be estimated as being 37Δ, and their average LET$_\infty$ can be estimated to be approximately 490 keV/μm. The apparatus used in these experiments did not allow clear identification of the particles in the peak region itself, where they are considerable smeared in both ionization and velocity. The relative contributions of fragments can be expected to vary rapidly in this region, and it is expected that work currently in progress will yield important information about these phenomena, especially in the spread, depth- dose curve. With these data, calculation of any desired measure of beam quality, for any beam configuration, should become practical. Some of the problems that become accessible to study are discussed by Curtis (1977).
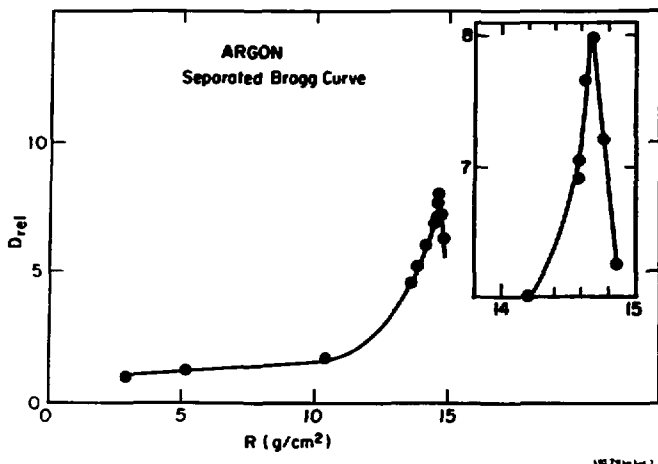
Fig. 29.   Separated Bragg curve for 525 MeV/nucleon argon ions.

ACKNOWLEDGEMENTS

REFERENCES

Alonso, J. R., Howard, J., and Criswell, T., 1979a, IEEE Trans. Nucl. Sci., NS-26: 3074.

Alonso, J. R. Tobias, C. A., and Chiu, W., 1979b, IEEE Trans. Nucl. Sci., NS-26: 3077.

BEVALAC, 1977, Bevatron/BEVALAC User's Handbook, Lawrenc Berkeley Laboratory Publication 101.

Blakely, E. A., Tobias, C. A., Yang, T. C. Smith, K. G., and Lyman, J. T., 1979, Radiat. Res., 80:122.

Crowe, K., Kanstein, L., Lyman, J. T., and Yeater, F., 1975, Lawrence Berkeley Laboratory Report LBL-4235 (unpublished).

Curtis, S. B., 1977, Int. J. Radiat. Oncol. Biol. Phys., 2: 87.

Dennis, J. A., 1972, in: "Proceedings, Third Symposium of Microdosimetry," H. G. Ebert, ed., Euratom, Luxembourg.

Epstein, J. W., Fernandez, J. I., Israel, H. H., Klarmann, J., and Newaldt, R. A., 1971, Nucl. Instr. Methods, 95: 77.

Gabor, G., Schimmerling, W., Greiner, D., Bieser, F., and Lindstrom, P., 1975, Nucl. Instr. Methods, 130: 65.

Goodman, L. J., and Colvett, R. D., 1977, Radiat. Res., 70: 495.

Greiner, D., 1972, Nucl. Instr. Methods, 103: 308.

ICRU, 1979, International Commission on Radiological Units and Measurements, "Average energy required to produce an ion pair," Report No. 31.

Kidd, J. M., Wefel, J. P., Schimmerling, W., and Vosburgh, K., 1979, Phys. Rev. C, 19: 1330.

Koehler, A. M., Schneider, R. J., and Sisterson, J. M., 1977, Med. Phys., 4: 297.

Lyman, J. T., and Howard, J., 1977a, in: "Biological and Medical Research with accelerated Heavy Ions at the BEVALAC, 1974-1977," Lawrence Berkeley Laboratory Report No. 330.

Lyman, J. T., and Howard, J., 1977b, Int. J. Radiat. Oncol. Biol. Phys., 3: 81.

Lyman, J. T., Howard, J., and Windsor, A. A., 1975, Fed. Phys., 2: 163 (abstract).

Myers, I. T., 1968, Ionization, in: "Radiation Dosimetry," F. H. Attix and W. C. Roesch, eds., Academic Press, New York.

Patrick, J. W., Stephens, L. D., Thomas, R. H., and Kelly, L. S., 1976, Health Phys., 30: 295.

Rossi, B., 1952, "High Energy Particles," Prentice Hall, Englewood Cliffs, N. J.

Schimmerling, W., Vosburgh, K. G., and Todd, P. W., 1973, Phys. Rev. B, 7: 2895.

Schimmerling, W., Vosburgh, K. G., Todd, P. W., and Appleby, A., 1976, Radiat. Res., 65: 389.

Schimmerling, W., Alonso, J., Morgado, R., Tobias, C. A., Grunder, H., Upham, F. T., Windsor, A., Amer. R. A., Yang, T. C. H., and Gunn, J. T., 1977a, IEEE Trans Nucl. Sci., NS-24: 1049.

Schimmerling, W., Curtis, S. B., and Vosburgh, Y. G., 1977b, Radiat. Res., 72: 1.

Silberberg, R., and Tsao, C. H., 1973, Astrophys. J. Suppl. Ser., 25: 315.

Skoski, L., Merker, M., and Shen, B. S. P., 1973, Phys. Rev. Lett., 30: 51.

Stephens, L. D., Thomas, R. H., and Kelly, L. S., 1976, Phys. Med. Biol. 21: 570.

Thomas, R. H., Lyman, J. T., and deCastro, T., 1978, Lawrence Berkeley Laboratory Report LBL-6710 (submitted to Radiat. Res).

Tobias, C. A., 1973, Radiology, 108: 145.

Vosburgh, K. G., 1973, Enciclopedia Della Scienza E Della Technica Mondadori, Annuario della EST, S and T, 17: 270.